Electronic Supplementary Material (ESI) for Materials Chemistry Frontiers.

SUPPORTING INFORMATION

Co(III) 2-ethylhexanoate, a Co(III) species with high solubility in a broad spectrum of solvents and precursor for the easy production of uniform coatings for water electrolysis and beyond

Gabriele Capilli[a], Thomas Szkopek[b], Marta Cerruti[a]

[a] *Department of Materials Engineering, McGill University, Montreal, QC H3A 0C5, Canada.*

[b] *Department of Electrical and Computer Engineering, McGill University, Montreal, QC H3A 2A7, Canada.*

Table of contents

1. Methods

1.1. Differential scanning calorimetry (DSC)

We performed DSCs with a DSC2500 analyzer (TA Instruments), on samples placed in Tzero aluminum pin hole hermetic pans, working at a heating/cooling rate of 10 °C min^{-1} in N_2 atm, and equilibrating the samples at –50 °C before the analysis.

Co(II) 2-ethylhexanoate (65 wt.% solution in mineral spirits, Co(II)eh) was dried in N_2 flux until it reached a hard waxy texture before introducing it in the pan. DSC cycle 1 for this sample consisted in heating from -50 °C to 220 °C then cooling back to -70 °C; DSC cycle 2 consisted just in heating from -70 °C to 200 °C.

Co(III) 2-ethylhexanoate (Co(III)eh) was dried in N_2 flux until it reached a highly viscous oily texture before introducing it in the pan. DSC cycle 1 for this sample consisted in heating from -50 °C to 200 °C then cooling back to -0 °C; DSC cycle 2 consisted in heating from -50 °C to 150 °C then cooling back to -70 °C, DSC cycle 3 consisted just in heating from -70 °C to 150 °C.

1.2. Thin film X-ray diffraction (XRD)

We analyzed the XRD patterns of the Co(III)eh-derived cobalt oxide thin films by means of a Bruker D8 Advance diffractometer (Bruker-AXS, Madison, USA) using a CuKα X-ray source ($\lambda = 1.54178$ Å, radiation operating at 40 kV and 40 mA) with a Nickel filter. The XRD setup was equipped with a LYNXEYE linear position sensitive detector (Bruker AXS, Madison, USA). The data were collected in the 2θ-range of 5.00–80.00° with increment of 0.02°.

1.3. Measurement of cobalt leakage by microwave plasma atomic emission spectroscopy

We prepared FTO/Co(III)eh, FTO/CoOx, and FTO/Co_3O_4 electrodes with area 1.4x2.5 cm (3.5 cm^2), according to the procedures reported in the Experimental section of the main article, and washed them with abundant DI water before testing. We immersed each electrode in 15 ml of 0.05 M KNO_3 electrolyte prepared from milliQ water and performed either 100 voltammetric cycles between 0.0 and +1.5 V vs Ag/AgCl or 8 hours of continuous electrolysis at +0.6 V vs Ag/AgCl. After cyclovoltammetry/electrolysis, we collected the electrolyte solutions, filtered them with a 0.45 µm pore size membrane (MilliporeSigma, USA), and added them with 2% v/v of HNO_3 70%.

We analyzed the cobalt release of the thin film electrodes in the 0.05 M KNO_3 electrolyte by means of microwave plasma atomic emission spectroscopy (Agilent 4210 MP-AES). We built the calibration curve from one blank and 5 reference solutions of 10 ppm, 5 ppm, 1 ppm, 0.5 ppm, and 0.1 ppm, obtained from dilution of a 1000 ppm Co standard solution in the same matrix chosen for the experiments (0.05 M KNO_3 + 2% v/v of HNO_3 70% in milliQ water).

The lowest value of the calibration curve, i.e. 0.1 ppm of Co (when excluding the blank), corresponds to a release of 7.3 nmol of cobalt per each cm^2 of thin film electrode surface. Indeed, 0.1 ppm = 1.5 µg of cobalt in 15 ml of electrolyte solution, 1.5 µg of cobalt = 25.5 nmol, which correspond to 25.5/3.5 = 7.3 nmol cm^{-2}. Concentration values below 0.1 ppm are reported as "<7 nmol cm^{-2}", because they are outside the linearity region even though they may be higher than the limit of detection of the method.

2. Results

2.1. Synthesis of Co(III)eh

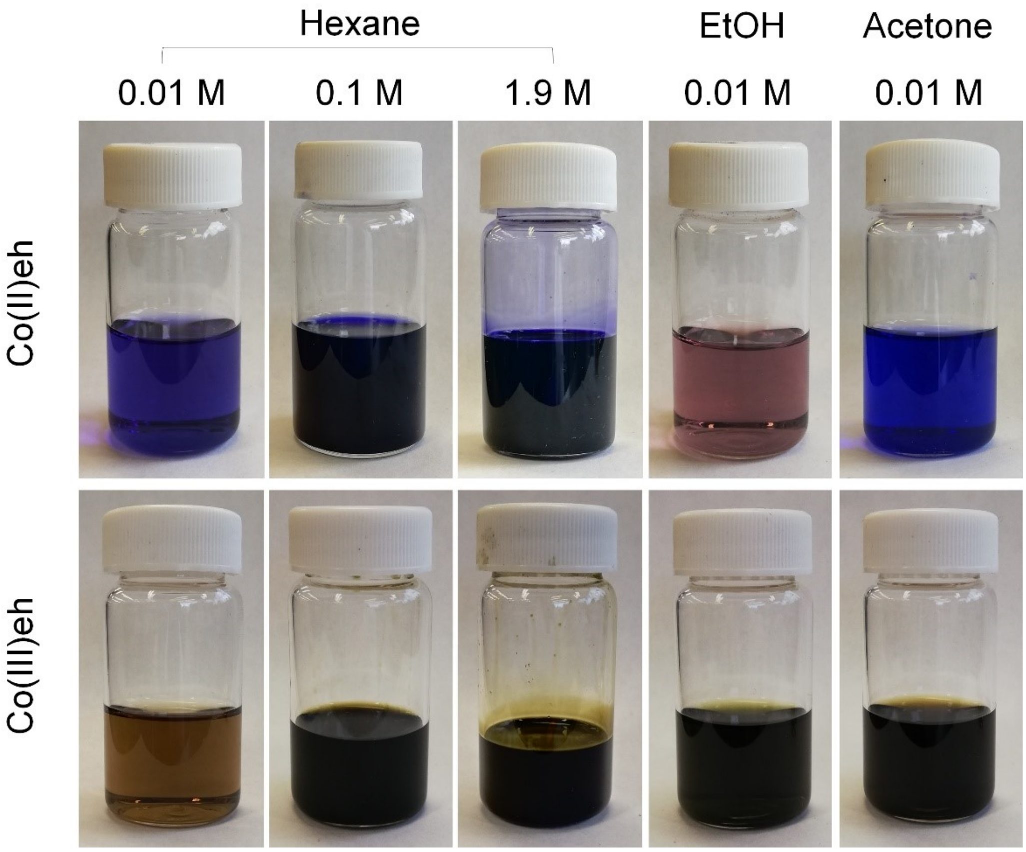

Fig. S1 Co(II)eh solutions in hexane (from commercial Co(II)eh in mineral spirit, see the Experimental Section of the main text), EtOH, and acetone (pure Co(II)eh synthesized, see the Experimental Section of the main text), and the corresponding Co(III)eh solutions after oxidation. The oxidation of Co(II)eh to Co(III)eh results in a marked colour change from pink, blue, or purple to green-brown.

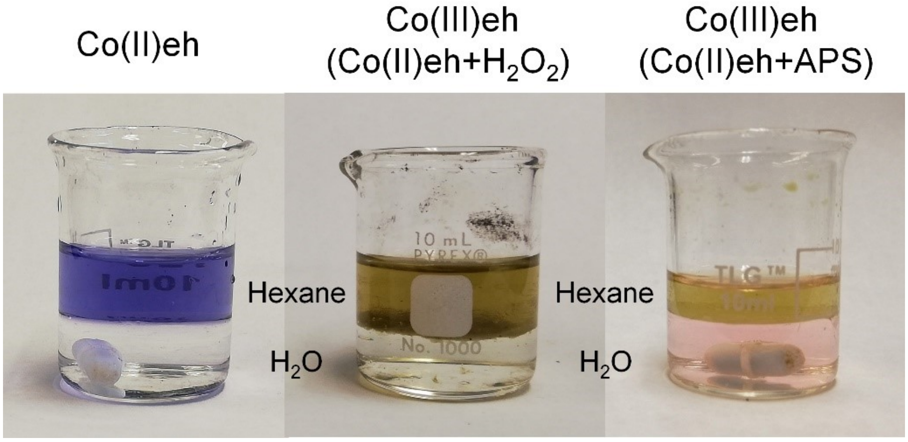

Fig. S2 Repartition in water/hexane of Co(II)eh (blue, left), Co(III)eh obtained after oxidation of Co(II)eh with H_2O_2 (green, middle), Co(III)eh obtained after oxidation of Co(II)eh with ammonium peroxydisulfate (APS) (green, right). The addition of a strong oxidizing agent like H_2O_2 or APS to Co(II)eh generates the same product Co(III)eh, with the same colour and solubility properties. The same solubility properties of Co(III)eh and its precursor exclude ligand substitutions in the coordination sphere of cobalt (e.g. H_2O instead of 2-ethylhexanoate) during its oxidation.

2.2. Solubility of Co(III)eh and Co(III)acetylacetonate (Co(III)acac)

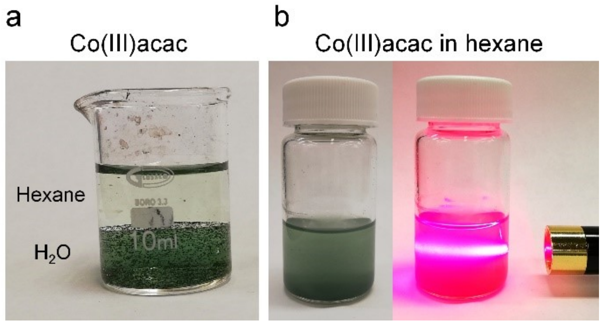

Fig. S3 (a) Co(III)acac partitioned in hexane/H_2O preferentially dissolves in water. (b) Dispersion Co(III)acac it hexane. Differently from Co(III)eh, Co(III)acac is insoluble in hexane, as shown by the Tyndall effect.

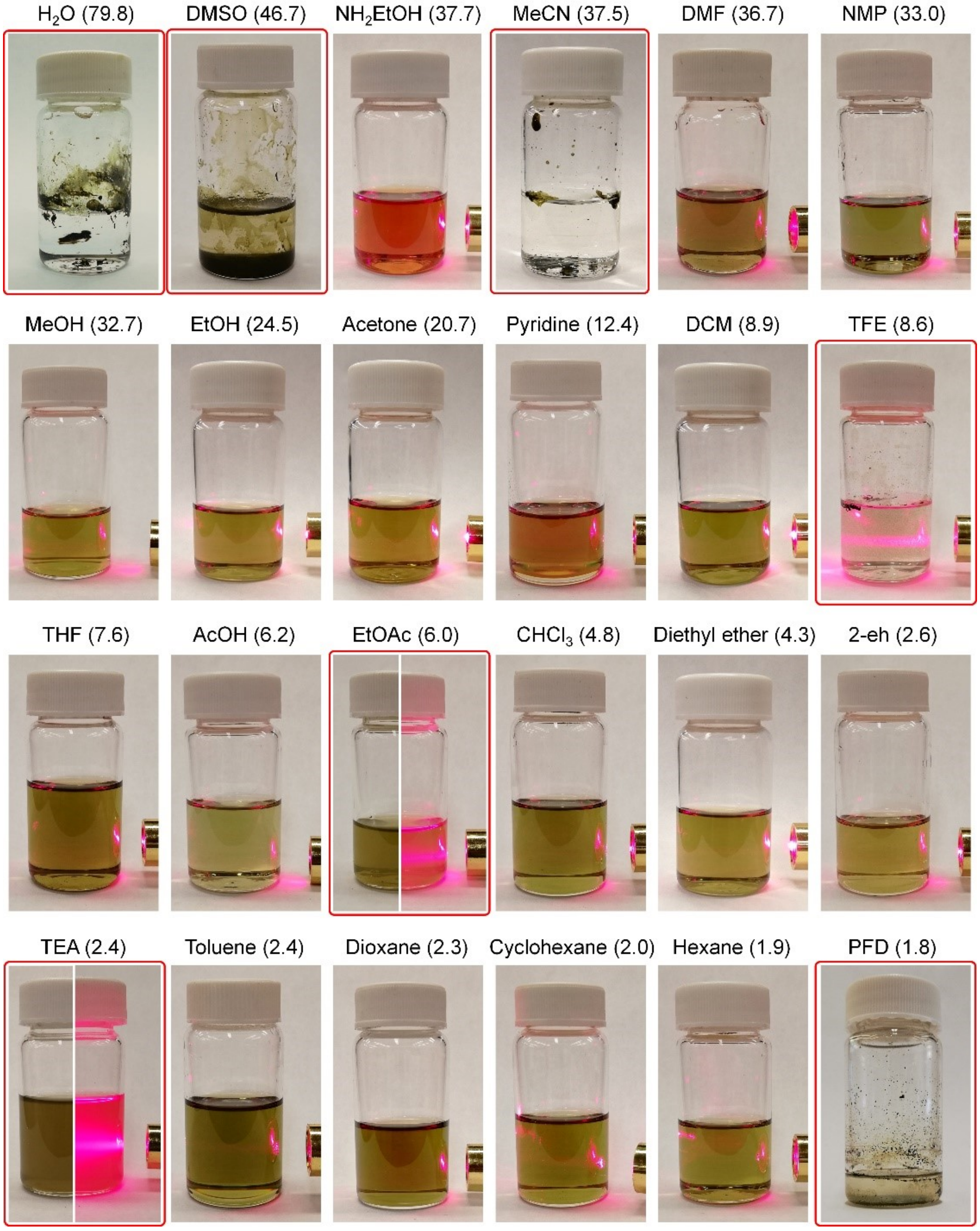

Fig. S4 Co(III)eh (synthesized) dissolved or dispersed in 24 solvents at 0.01 M concentration. We show the results obtained in solvents from the highest to lowest dielectric permittivity (ε, reported in parenthesis after the solvent name). The solvents where Co(III)eh is insoluble, partially soluble, or suspendable are highlighted with red squares. A laser pointer is shown in most pictures to show complete (no Tyndall effect) or incomplete (Tyndall effect) solubility.

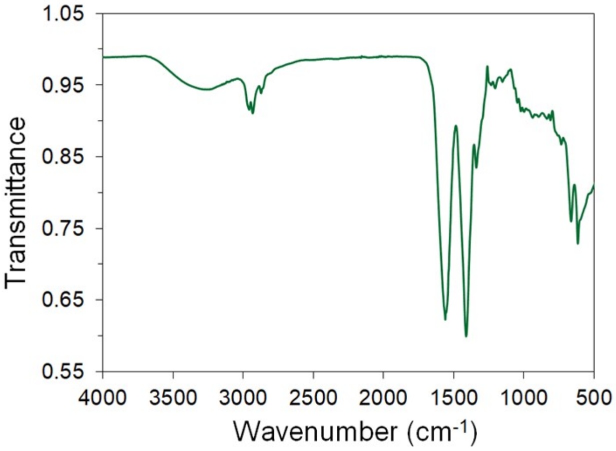

Fig. S5 FTIR spectrum of the precipitate formed after 1-hour dissolution of Co(III)eh in triethylamine (TEA, ε = 2.4). The spectrum is remarkably different from that of Co(III)eh (see Figs. 2b and S7), implying that a chemical transformation happened after dissolution. The precipitate is potentially the 2-eh–TEA ammonium salt derived from the reaction of the solvent, TEA, with the 2-eh ligands displaced from Co(III)eh by TEA. Any further characterization of this process and product is out of the scope of this work.

2.3. Characterization of Co(III)eh

2.3.1. DSC

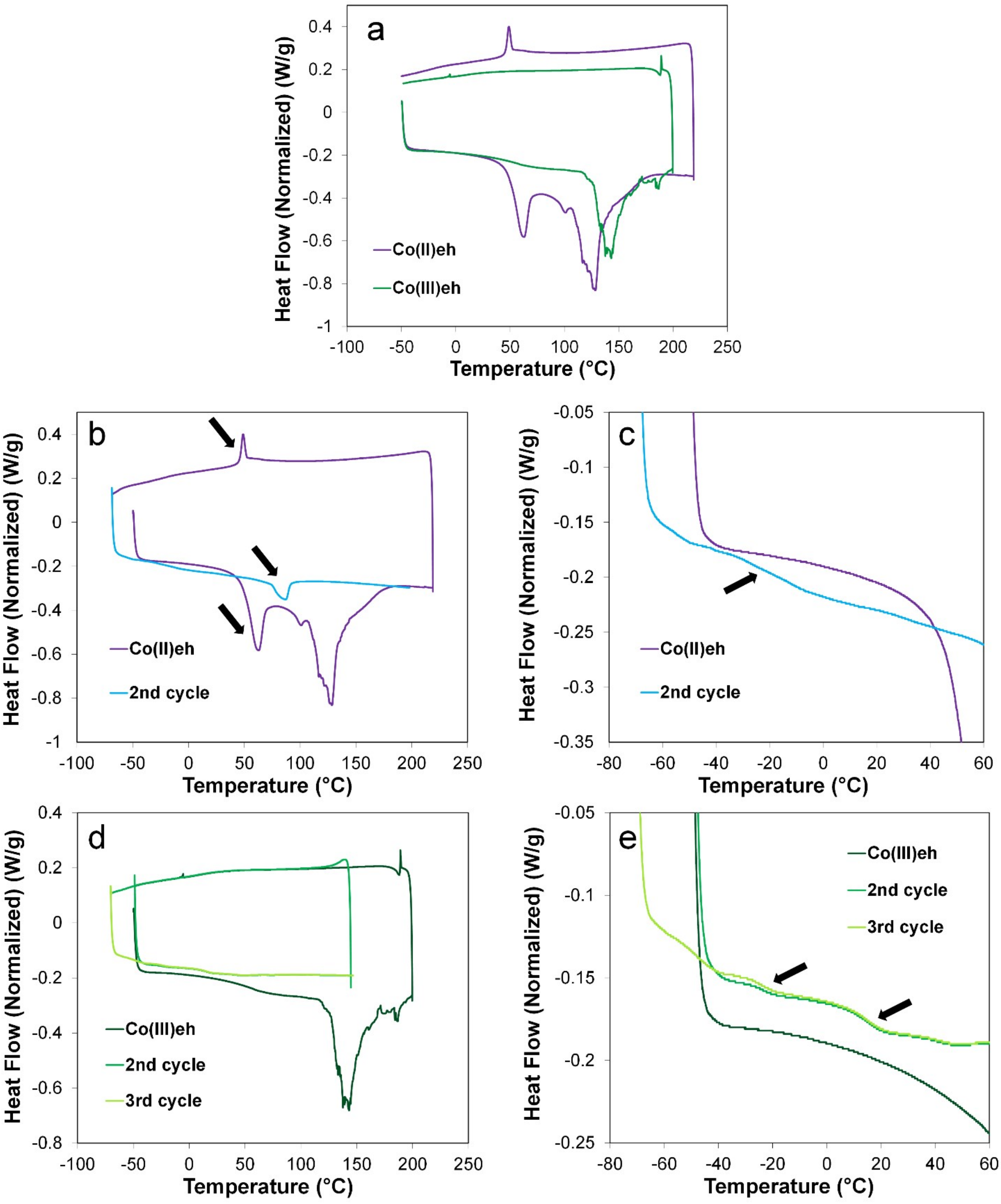

Fig. S6 DSCs of (a) Co(II)eh and Co(III)eh (commercial). (b, c) Details of the 2 DSC cycles carried out on Co(II)eh. (d, e) Details of the 3 DSC cycles carried out on Co(III)eh.

As shown in Fig. S6a, during the first DSC scan both Co(II)eh (commercial, see the Experimental Section of the main text) and Co(III)eh show an irreversible peak above 100 °C, with a complex shape due to probably several phenomena happening at the same time, i.e. evaporation of the mineral spirit residue, reduction of

Co(III) to Co(II) (in the case of Co(III)eh), and partial decomposition of the complexes, which starts at the same temperatures observed during the thermogravimetric analyses (Fig. 2d in the main text).

Co(II)eh shows a melting/crystallization transition between 50 and 70 °C (see arrows in panel b), which is absent in Co(III)eh (panel d), and a glass transition at –25 °C (see arrow in panel c). The Co(III)eh sample, instead, shows just 2 small glass transitions, reproducible after 2 subsequent cycles, respectively at –25 and +15 °C (see arrows in panel e).

These observations are in agreement with the step-wise melting mechanism (i.e. the presence of multiple pre-melting transitions instead of a single melting point or glass transition) reported in the literature for carboxylates of several metal ions, such as Li(I), Na(I), K(I), Ag(I), Co(II), Zn(II), Cu(II), Pb(II), Ce(III), and La(III).[1-4]

2.3.2. Fourier transform Infrared spectroscopy (FTIR)

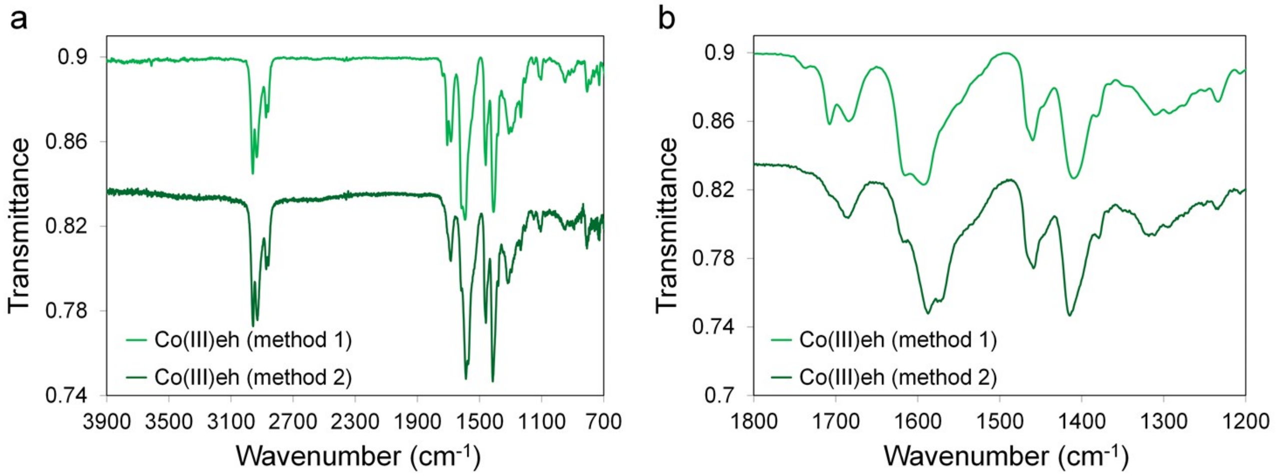

Fig. S7 (a) FTIR spectra of Co(III)eh samples (from both commercial and synthesized Co(II)eh) and (b) zoom-in in the carboxylate stretching region. The ν_{as}COO of Co(III)eh from commercial Co(II)eh consists of 3 components centered at 1617, 1587, and 1571 cm^{-1}, the middle one being the most intense. The ν_{as}COO of Co(III)eh from synthesized Co(II)eh has 2 main components only, at 1617 and 1587 cm^{-1}, the second one being again the most intense.

Table S1 Frequency, expressed in cm^{-1}, and assignment of main infrared absorption bands for 2-eh, Co(II)eh, and Co(III)eh.

Frequency of main bands (cm^{-1})			Vibrational assignment
2-eh	Co(II)eh	Co(III)eh	
2961	2959	2958	$\nu_{as}CH_3$
2938	2925	2930	$\nu_{as}CH_2$
2877	2873	2873	$\nu_{s}CH_3$
2860	2858	2859	$\nu_{s}CH_2$
1705	(1685)	(1706)	νC=O, carboxylic C=O stretching that in Co(II)eh and in Co(III)eh results from small amounts of free 2-eh present as impurities
		(1684)	
		1617	ν_{as}COO
	1585	1587	
	1548	1571	
1462	1459	1458	δCH_2
1415	1420	1414	ν_{s}COO
(1385)	(1378)	(1378)	
	(1319)	(1317)	Multiple νC–C and νC–O bands from the ligand structure
1289	1296	1293	
(1272)			
1228	(1236)	(1234)	
(1205)	(1208)	(1207)	
940			Vibration of the 2-eh–2-eh dimer, absent in both Co complexes

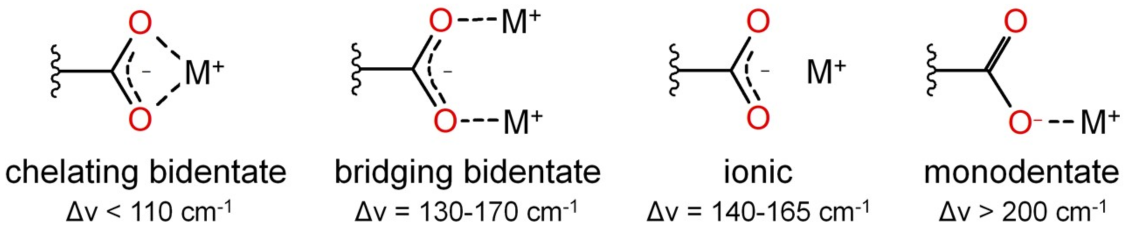

Fig. S8 Types of M–L coordination in metal-organic carboxylates and corresponding Δν, i.e. the difference between the frequencies of the ν_{as}COO and ν_{s}COO vibrations in their infrared spectra.

Carboxyl groups can act as uni- or bi-dentate ligands; in the latter case, they can either chelate a positive ion or act as a bridge between two ions.[5] The type of metal–carboxylate bond depends on the properties of the metal center, such as radius, valence, and hard/soft character. A larger difference between the ν_{as}COO and ν_{s}COO infrared vibrations corresponds to a more asymmetrical interaction between the carboxylate group and the metal center.[5-7]

The monodentate coordination, where only one carbonyl oxygen interacts with the metal, removes the equivalence of the C–O bonds. This results in an increase of the ν_{as}(COO) frequency and intensity (one of the C–O bonds shows an enhanced double-bond character) and a corresponding decrease of the ν_{s}(COO) frequency and intensity.[5-7] Co–carboxylate coordination in Co(III)eh is most likely not monodentate since the intensities of ν_{s}(COO) and ν_{as}(COO) are similar.

2.4. Co(III)eh, Co(III)acac, and Co(NH_3)$_5$$H_2O$]($NO_3$)$_3$ coatings

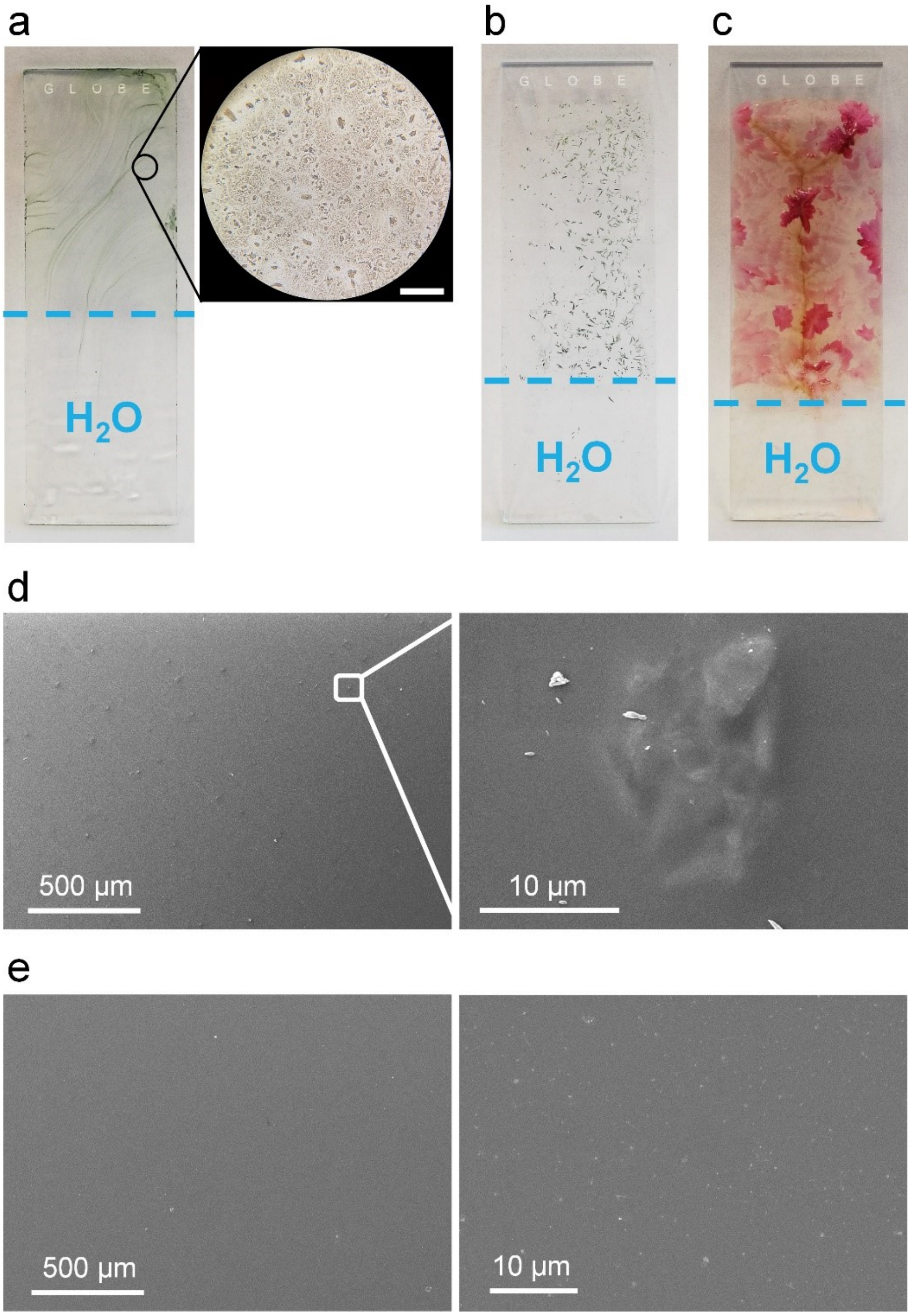

Fig. S9 Digital photos and optical microscopy images of Co(III)acac coatings deposited on glass from (a) toluene and (b) EtOH solutions. Scale bar of the optical micrograph: 500 µm. (c) Coating of [Co(NH_3)$_5$$H_2O$]($NO_3$)$_3$ on glass, which crystallizes and transforms to its corresponding Co(II) salt during air exposure. In all images, the areas below the dashed blue line were immersed in water for 10 s. (d) Scanning electron micrographs of a Co(III)eh (commercial) coating on glass and of a microscopic surface defect (~10 µm in size) which form on the surface of the Co(III)eh coating right after its deposition. (e) Scanning electron micrographs of a Co(III)eh coating on a thin glass slide for optical microscopy, with lower surface roughness compared to the glass support used in panel d.

The surface investigation of Co(III)eh coatings through optical and SEM microscopy (Figs. 3b, inset, and S9d) reveals the presence of regularly dispersed microscopic surface defects, i.e. agglomerates and/or microscopic collapsed bubbles. These most likely form in correspondence of surface defects and dust particles entrapped during film drying in environmental conditions. The size of the micro-defects formed on Co(III)eh coatings deposited on a substrate with lower surface roughness is remarkably lower (<1 µm in Fig. S9e vs ~10 µm in Fig. S9d). This result suggests these defects are affected by the surface topography of the support chosen.

Photochemical stability of Co(III)eh and Co(II)eh

Table S2 Elemental composition measured by XPS on the surface of Co(III)eh and Co(II)eh films before and after UVA-Vis and UVC irradiation. Values represent mean ± SD (in parentheses) calculated for 3 independent samples, on 2 different spots per sample.

	Atomic % (XPS)		
	C1s	**O1s**	**Co2p**
Co(II)eh room T	71 (3)	22 (3)	7 (2)
Co(II)eh UVA 15 suns, 1 h	55 (4)	34 (3)	11 (3)
Co(II)eh UVC, 1 h	52 (4)	35 (5)	13 (3)
Co(III)eh room T	70 (4)	24 (2)	6 (1)
Co(III)eh UVA 15 suns, 1 h	65 (4)	29 (3)	6 (2)
Co(III)eh UVC, 1 h	59 (5)	33 (4)	8 (2)
Co_3O_4 bulk	15 (3)	57 (2)	28 (2)

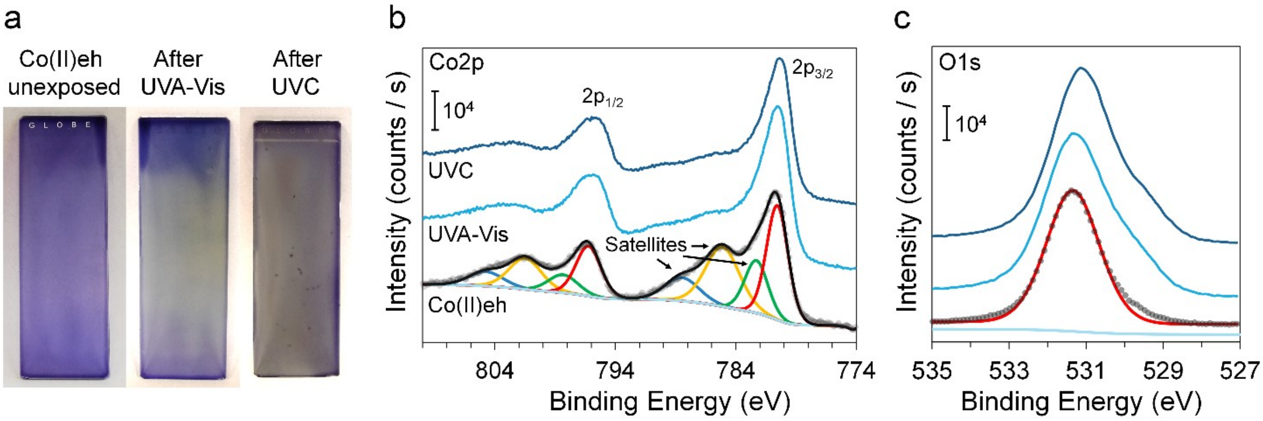

Fig. S10 (a) Digital photographs of Co(II)eh coating (commercial, coverage: 6 µmol cm^{-2}) before and after irradiation under intense UVA-visible and UVC light (see the Experimental Section of the main text). Co(II)eh is a photolabile species and undergoes chemical transformation under both light sources. Representative high resolution (b) Co2p and (c) O1s XPS spectra collected on the films shown in (a). Experimental data are shown as transparent grey dots, individual component fits are in colour and the overall fit in black solid line for the spectra of the unexposed films, whereas only the experimental data is shown in solid colour lines for the UVC and UVA-Vis treated samples.

For 3d transition elements such as cobalt, the most informative parameters to determine the metal electronic state through XPS analysis are the Co2p$_{1/2}$ – Co2p$_{3/2}$ spin-orbit splitting (ΔE) and the ratio between the intensities of the Co 2p$_{3/2}$ peak and its satellites ($\Sigma I_{sat}/ICo_{2p3/2}$).[8] In paramagnetic Co(II) complexes ΔE is approximately 16 eV while in diamagnetic Co(III) compounds it is close to 15 eV. Shake-up processes are significant only in paramagnetic high-spin Co(II) complexes; the transition to a low-spin state causes the suppression of the satellite: $\Sigma sat/ICo_{2p3/2}$ of Co(III) complexes is usually half of the corresponding Co(II) ones.[8]

The high resolution (HR) O1s XPS spectra of Co(III)eh films (Fig. 3g in the main text) show one main peak (red fit) with E_b shifting from 531.2 eV to 531.0 eV and 530.9 eV after UVA-Vis and UVC irradiation, respectively. This peak corresponds to the organic carboxylic group of the ligand. The strong light irradiation generates a shoulder peak centered at 529.2 eV (green fit) that can be assigned to oxygen in cobalt oxides and indicates a minimal conversion of Co(III)eh under these conditions.

Co(II)eh is not as stable as Co(III)eh under the same irradiation conditions, as shown by the film colour change after exposure to UVA-Vis and UVC light (Fig. S10a). In the HR Co2p XPS spectrum of Co(II)eh (Fig. S10b), the intense satellite peaks ($\Sigma I_{sat}/ICo_{2p3/2} = 1.4$) and the high ΔE value of 15.8 eV (E_b of Co2p$_{1/2}$ and Co2p$_{3/2}$ peaks, red fit, are respectively 780.2 and 796.0 eV) clearly indicate the presence of high-spin Co(II). After both UVA-Vis and UVC exposure, the satellites in the Co2p spectrum are drastically attenuated and the Co 2p$_{1/2}$ E_b shifts from 796.0 to 795.2 eV (ΔE reduces from 15.8 to 15.0 eV), in accordance with a transition to a Co(III) state. The HR O1s XPS spectra of Co(II)eh films (Fig. S10c) show that the irradiation conditions chosen cannot degrade the carboxylic ligand, i.e. they induce almost no formation of cobalt oxide phases, as also confirmed by the elemental composition values reported in Table S2.

2.6. Co(II)eh- and Co(III)eh-derived cobalt oxide thin films and patterns

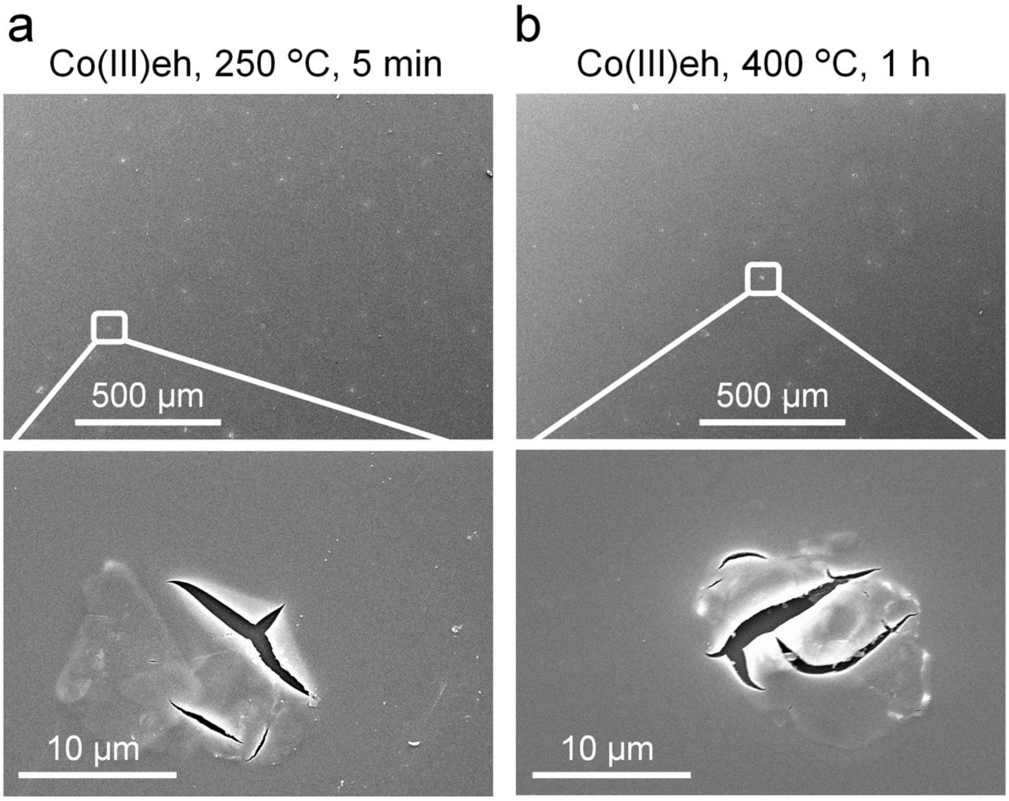

Fig. S11 Scanning electron micrographs of the surface of Co(III)eh-derived cobalt oxide coatings on glass obtained after (a) 5 min heating at 250 °C and (b) 1 hour heating at 400 °C, together with higher magnification micrographs of the microcracks which form on the coating surface during the thermal treatment, in correspondence of the microscopic defects observed in Fig. S9d.

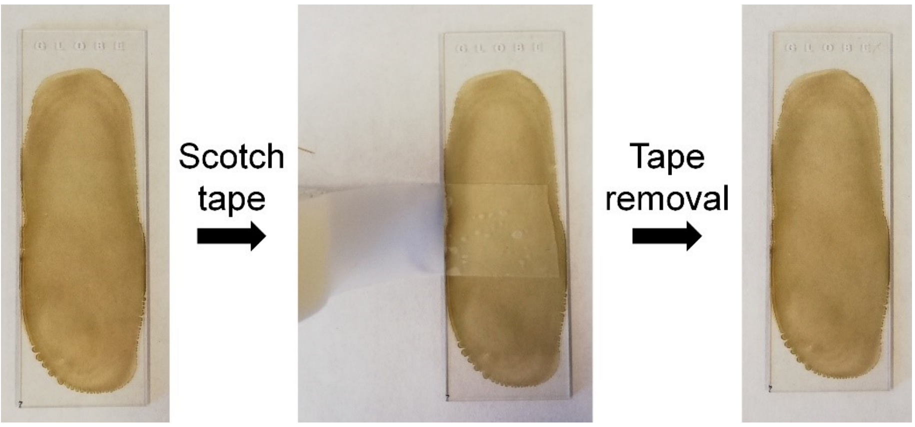

Fig. S12 Scotch tape test on a cobalt oxide film formed on glass from a Co(III)eh solution in hexane after heating to 250 °C for 5 minutes.

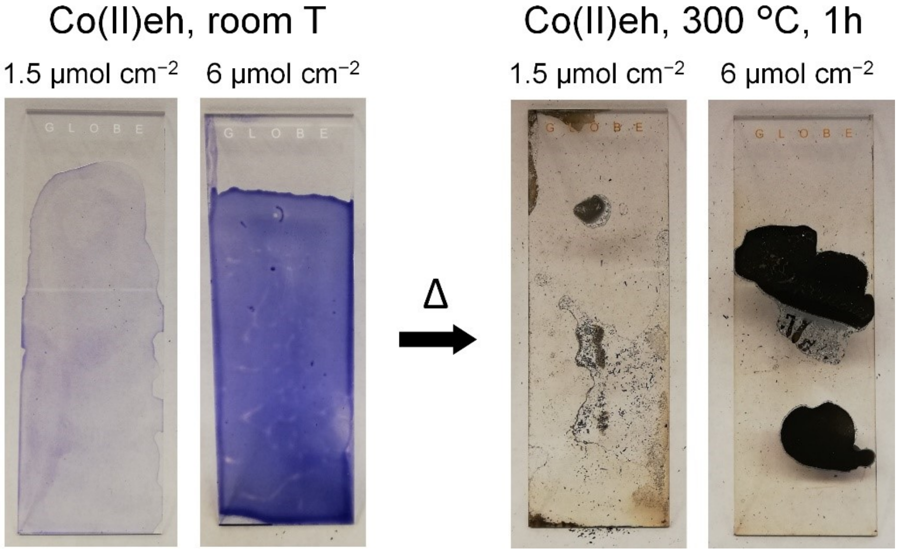

Fig. S13 Thermal conversion of 2 Co(II)eh (commercial) films of different thicknesses: 1.5 µmol cm^{-2} and 6 µmol cm^{-2}. Heating the coatings to 300 °C for one hour leads to the formation of Co_3O_4 domains which easily detach from the substrate.

2.6.1. XPS analysis of Co(III)eh and Co(III)eh-derived cobalt oxide thin films

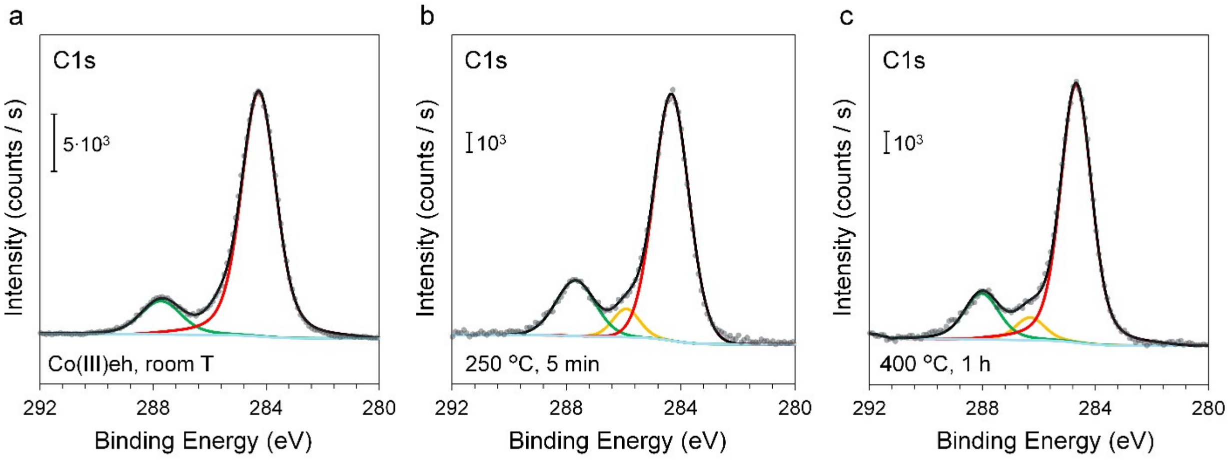

Fig. S14 High-resolution C1s XPS spectra of (a) Co(III)eh and (b, c) Co(III)eh-derived cobalt oxide thin films on glass, produced by thermal annealing at (b) 250 °C for 5 min, and (c) 400 °C for 1 hour. Experimental data are shown as transparent grey dots, individual component fits are in colour, and the overall fit is in black solid line.

The HR C1s XPS spectrum of a Co(III)eh thin film (Fig. S14a) is characterized by 2 components centered at 284.3 eV and 287.7 eV, which can be ascribed to the sp^3 carbon atoms in the hydrocarbon ligand chains and adventitious carbon from the atmosphere (red fit), and the carboxylic –COO$^-$ heads of the ligands (green fit). A significant amount of adventitious carbon contamination occurs on the surface of every sample exposed to air which is not sputtered with Ar ions before analysis. We did not perform any ion bombardment to prevent the chemical reduction of the films.

The HR C1s XPS spectra of cobalt oxide thin films formed upon thermal annealing of Co(III)eh at 250 °C (Fig. S14b) and 400 °C (Fig. S14c) are almost identical and their intensity is remarkably lower compared to that of Co(III)eh. The main component, centered at 284.4 eV and 284.8 eV (red fit), respectively, corresponds to the contamination from atmospheric adventitious carbon. Likewise, the small component centered at 286.2 eV (yellow fit) most likely corresponds to C–O species in the adventitious carbon contamination. Finally, the component centered at 287.8 eV (green fit), most likely arises from surface cobalt carbonate naturally formed on the cobalt oxide films exposed to the atmosphere during the high-temperature treatments, or to -COO from ligand traces, in the sample treated at 250 °C.

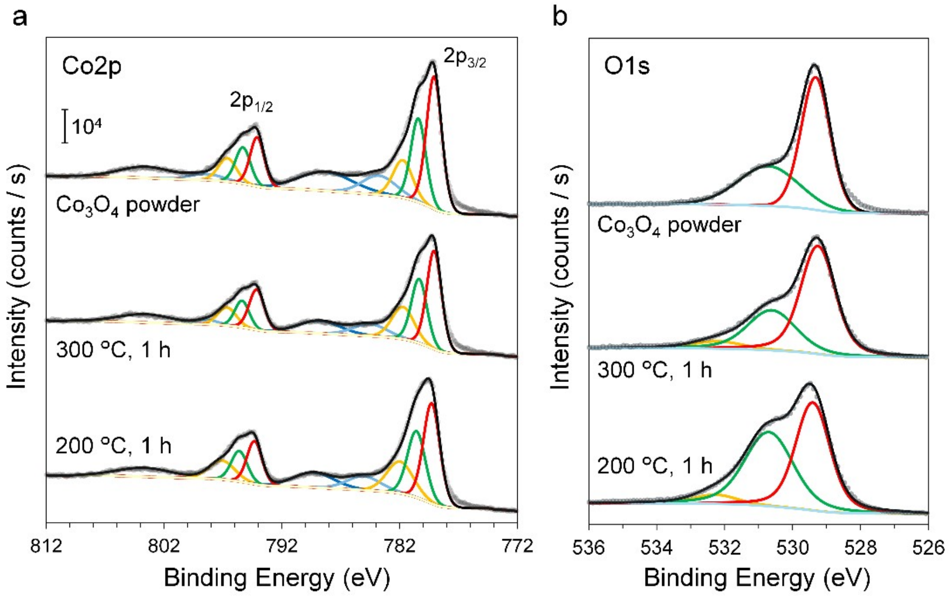

Fig. S15 High resolution (a) Co2p and (b) O1s XPS spectra of Co_3O_4 powder and cobalt oxide films on glass, produced by thermal annealing of Co(III)eh films at 200 °C for 1 hour and at 300 °C for 1 hour. Experimental data are shown as transparent grey dots, individual component fits are in colour, and the overall fit is in black solid line.

Table S3 Binding energy (in eV) of the HR Co2p and HR O1s XPS peaks components of all the materials discussed in this work.

Compound	**$Co2p_{3/2}$ peaks (eV)**					**$Co2p_{1/2}$ peaks (eV)**				**O1s peaks (eV)**		
	1	**2**	**3**	**4**	**5**	**1**	**2**	**3**	**4**	**1**	**2**	**3**
Co(II)eh room T	780.2	782.3	785.4	788.3		796.1	798.3	801.7	804.8	531.3		
Co(II)eh UVA, 1 h	780.1	782.3	788.1			795.5	797.5	802.4		529.5	531.3	
Co(II)eh UVC, 1 h	780.1	782.3	788.1			795.5	797.5	802.4		529.4	531.0	
Co(III)eh room T	780.2	782.3	786.7			795.6	797.1	802.0		531.2		
Co(III)eh UVA, 1 h	780.0	782.0	786.9			795.2	797.0	802.9		529.3	531.0	
Co(III)eh UVC, 1 h	780.0	782.0	786.9			795.2	797.0	802.9		529.2	530.9	
Co oxide 250°C, 5 min	779.4	780.1	782.0	785.3	789.6	794.3	795.7	796.8	804.1	529.2	531.0	532.2
Co oxide 200°C, 1 h	779.5	780.1	782.0	784.2	789.5	794.3	795.7	796.8	804.2	529.3	530.8	532.3
Co oxide 300°C, 1 h	779.4	780.1	782.0	785.0	789.5	794.3	795.6	796.8	804.0	529.2	530.9	532.3
Co oxide 400°C, 1 h	779.3	780.1	782.0	785.5	798.7	794.3	795.6	796.8	803.6	529.2	531.0	
Co_3O_4 bulk	779.4	780.1	782.0	785.3	789.6	794.3	795.6	796.8	804.0	529.2	531.0	

2.6.2. XRD analysis of Co(III)eh-derived cobalt oxide thin films

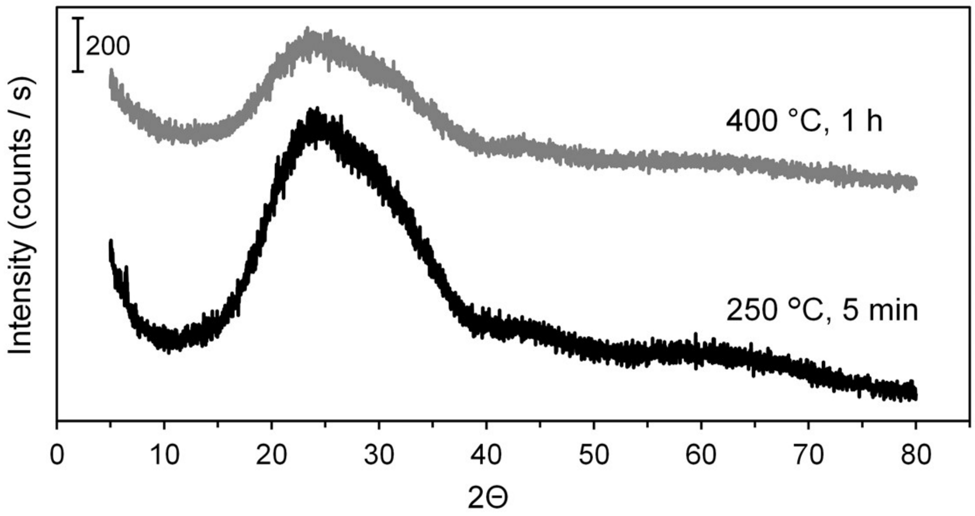

Fig. S16 XRD patterns of two Co(III)eh-derived cobalt oxide thin films on glass, produced by thermal annealing at 250 °C for 5 min, and 400 °C for 1 hour. The broad peak at 2Θ = 24° arises from the glass substrate. The absence of detectable diffraction peaks demonstrates the amorphous nature of the coatings produced in those conditions.

2.6.3. Laser-induced formation of cobalt oxide patterns on Co(III)eh and Co(II)eh

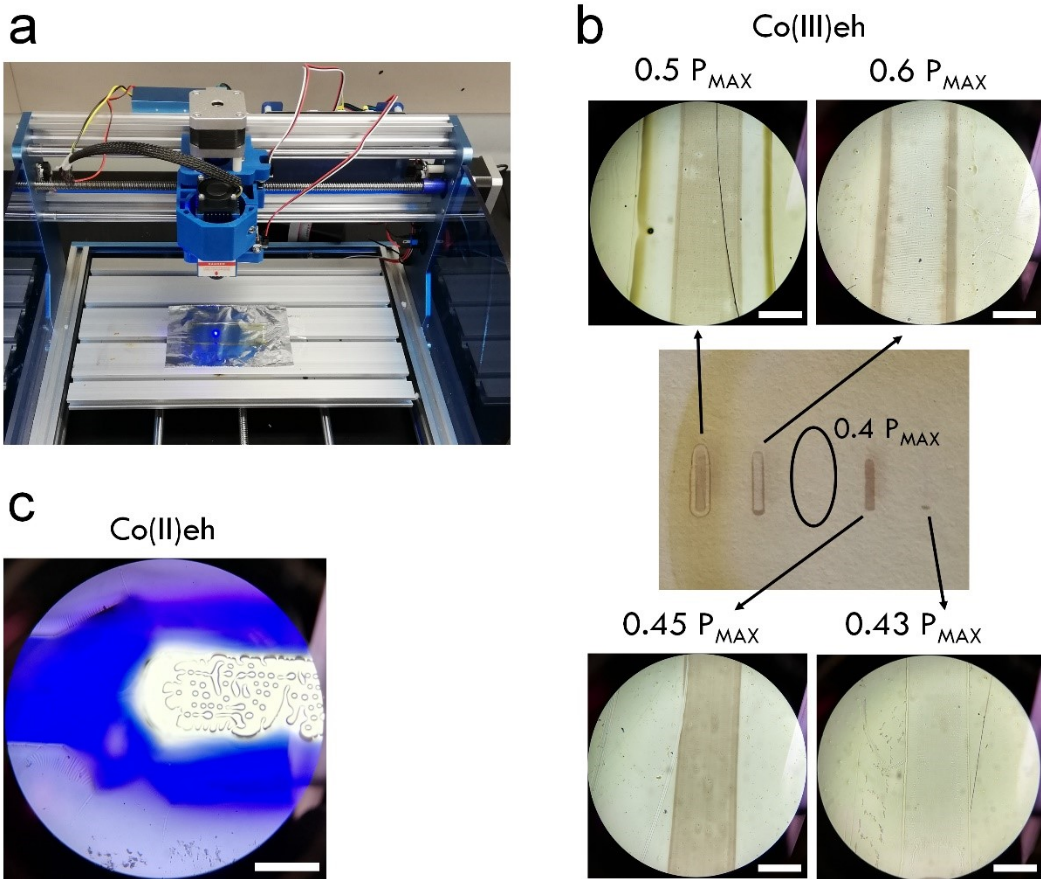

Fig. S17 (a) Laser engraver mounted on the computer numerical control (CNC) machine used to draw Co_3O_4 patterns on Co(III)eh films. (b) Digital image (center) and optical microscopy pictures of 4 tracks drawn on a Co(III)eh (commercial) film by operating the laser at 4 different power levels, i.e. 50%, 60%, 0.45%, and 0.43% of its maximum working power (5.5 W). (c) Optical microscopy image showing the effect of laser beam irradiation on a film of Co(II)eh (synthesized). Under the heat of the laser beam, Co(II)eh suddenly melts and migrates toward the colder edges of the projected beam, where it solidifies again without undergoing any degradation. Scale bars in all images: 500 µm.

2.7. Electrochemical characterization of Co(III)eh-derived cobalt oxide thin films

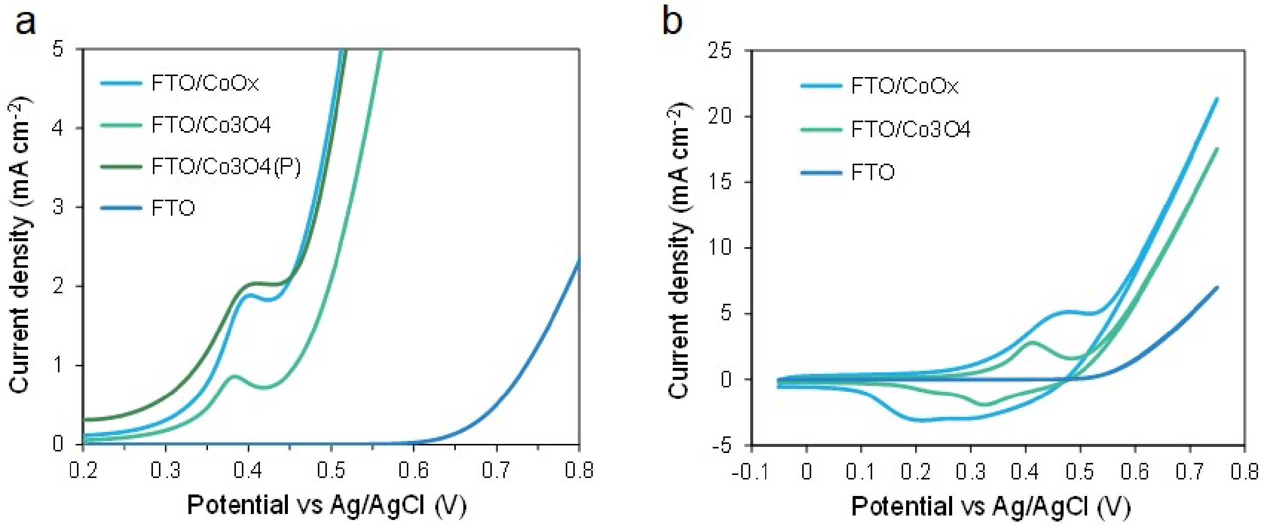

Fig. S18 (a) Linear sweep voltammetry scans of FTO/CoOx (light blue), FTO/Co_3O_4 (light green), FTO/Co_3O_4(P) (green), and bare FTO (blue) electrodes; scan rate = 10 mV s^{-1}. Measurements performed in 1 M KOH(aq) electrolyte, in N_2 atmosphere, reference electrode: Ag/AgCl. (b) Cyclic voltammograms of FTO/CoOx (light blue), FTO/Co_3O_4 (light green), and bare FTO (blue) electrodes. Co_3O_4 shows one reversible oxidation state transition, centered at E = +0.38 V, while CoOx can be oxidized at E = +0.45 V and reversibly reduced through a 2 step process (2 broad reduction peaks at E = +0.3 and +0.2 V). Subsequent cycles over the -0.5 – +0.75-V range leads to superimposable scans. Data were recorded at a scan rate of 50 mV s^{-1}, in 0.1 M KOH.

The setup used to carry out the water oxidation experiment and to measure the amount of O_2 evolved (described in the Experimental Section of the main text) corresponds to a so-called 'continuously stirred tank reactor under flow'. This configuration exhibits several advantages, such as reducing the continuous increase of O_2 inside the cell that inevitably comes from small leaks and would increase the error in the measurement of the net O_2 produced. Also, working under steady-state conditions allows to directly convert the O_2 concentration measured to the rate of O_2 production, without needing corrections for the O_2 partition between the liquid and the gas phases (Henry's law).

The anode compartment is bubbled with a constant N_2 flux (30 mL min^{-1}); the electrolyte volume and the headspace are both 30 mL. We manually sample the 1 ml of the cell headspace every 30 min (see the Experimental Section of the main article for more details). The minimum detectable O_2 concentration with our GC method is 5 ppm (5 µL L^{-1} = 210 nmol L^{-1} in std conditions, according to the ideal gas law PV = nRT). Under N_2 flow of 30 mL min^{-1}, this value corresponds to a minimum rate of O_2 production of 0.15 µL min^{-1} (0.38 µmol h^{-1}). The O_2 production rates measured during the chronoamperometric tests are around 100 µL min^{-1}, far above the detection limit.

The µmol of O_2 produced over time, reported in Fig. 6d, are calculated by integrating over time the O_2 production rates measured every 30 min. The O_2 production rate is calculated by the formula: v_{O2} [µmol min^{-1} cm^{-2}] = C_{O2} [µL L^{-1}] × 10^{-3} [L mL^{-1}] × j [mL min^{-1}] / (A [cm^2] × 22.4 [µL µmol^{-1}]), where C_{O2} is the O_2 concentration measured through GC, j the N_2 flux (30 mL min^{-1}), and A the geometric area of the electrode (2.5 cm^2).

The faradaic efficiency is calculated as the ratio of (4 × moles of O_2 generated) / (moles of electrons flowed through the circuit) = (4 × v_{O2} [mol s^{-1} cm^{-2}]) / (A [cm^2] × i [C s^{-1}] / F [C mol^{-1}]), where A is the geometric area of the electrode, F is the Faraday constant, and i the current measured during the chronoamperometry (Fig. 6c).

2.8. Co leakage from Co(III)eh and Co(III)eh-derived cobalt oxide thin films

Table S4 Cobalt leakage from a Co(III)eh coating deposited on FTO and two Co(III)eh-derived cobalt oxide thin films on FTO produced, respectively, by thermal annealing at 250 °C for 5 min and 400 °C for 1 hour. The electrode leakage is measured after 100 voltammetric cycles in the 0.0-1.5 V vs Ag/AgCl potential range and after 8 h of continuous electrolysis at +0.6 V vs Ag/AgCl (just the cobalt oxide thin films). The second column reports the concentration of dissolved cobalt measured in the electrolyte solutions used for the leakage tests (see method section of this document, paragraph 1.3). In the third column, the values from the second column are converted into values of cobalt leakage per unit area of electrode tested.

Sample	**[Co]$_{340.512\ nm}$ (ppm)**	**Coating leakage (nmol$_{Co}$ cm^{-2})**
Co(III)eh, 100 CV	0.02	<7
250 °C, 100 CV	0.94	68.6
250 °C, 8h electrolysis	0.21	15.3
400 °C, 100 CV	0.35	25.6
400 °C, 8h electrolysis	0.06	<7

The cobalt leakage from the electrodes tested (see method section, paragraph 1.3) is negligible. In the case of Co(III)eh), the leakage is <7 nmol of cobalt per cm^2 of electrode area, i.e. close to the detection limit of the analytical method adopted. The Co(III)eh-derived cobalt oxide films produced by thermal annealing at 400 °C show a ~2-fold lower cobalt leakage compared to that of cobalt oxide films produced at 250 °C.

2.9. Electrochromic behaviour of Co(III)eh-derived cobalt oxide thin films

Fig. S19 Electrochromic effect of a FTO/CoOx electrode subjected to a potential of +0.5 V vs Ag/AgCl in a 1 M KOH solution.

3. References

1. S. Mishra, S. Daniele, L. G. Hubert-Pfalzgraf, Metal 2-ethylhexanoates and related compounds as useful precursors in materials science, *Chem. Soc. Rev.*, **2007** (36) 1770-1787.
2. P. N. Nelson, R. A. Taylor, Theories and experimental investigations of the structural and thermotropic mesomorphic phase behaviors of metal carboxylates, *Appl. Petrochem. Res.*, **2014** (4) 253-285.
3. H. Kambe, T. Ozawa, M. Onoue, S. Igarashi, Physicochemical Studies on Cobalt Salts of Higher Fatty Acids. VI. Some Observations on Thermal Transitions of Cobalt Soaps, by Differential Thermal Analysis, Thermogravimetry, and Magnetic Measurement, *Bull. Chem. Soc. Jpn.*, **1962** (35) 81-85.
4. S. Morlens, L. Ortega, B. Rousseau, S. Phok, J. L. Deschanvre, P. Chaudouet, P. Odier, Use of cerium ethylhexanoate solutions for preparation of CeO_2 buffer layers by spin coating, *Mater. Sci. Eng., B*, **2003** (104) 185-191.
5. K. Nakamoto, P.J. Mc Carty, Spectroscopy and Structure of Metal Chelate Compounds, *Wiley*, New York, **1968**. p. 268 et seq.
6. J. Simon-Kutscher, A. Gericke, H. Hühnerfuss, Effect of Bivalent Ba, Cu, Ni, and Zn Cations on the Structure of Octadecanoic Acid Monolayers at the Air−Water Interface As Determined by External Infrared Reflection−Absorption Spectroscopy, *Langmuir*, **1996** (12) 1027-1034.
7. P. N. Nelson, H. A. Ellis, N. A. S. White, Solid state ^{13}C-NMR, infrared, X-ray powder diffraction and differential thermal studies of the homologous series of some mono-valent metal (Li, Na, K, Ag) n-alkanoates: a comparative study, *Spectrochim. Acta A*, **2015** (145) 440-453.
8. T. Ivanova, A. Naumkin, A. Sidorov, I. Eremenko, M. Kiskin, X-ray photoelectron spectra and electron structure of polynuclear cobalt complexes, *J. Electron Spectrosc. Relat. Phenom.*, **2007** (156-158) 200-203.